DOI: 10.1016/S1872-5813(22)60036-7

Post-functionalization of graphitic carbon nitride for highly efficient photocatalytic hydrogen evolution

YANG Yi-long[1,*], LI Shan-ying[1], MAO Yan-li[2], DANG Li-yun[1], JIAO Zhuo-fan[1], XU Kai-dong[1,*]
（1. *School of Materials and Chemical Engineering*, *Henan University of Urban Construction*, *Pingdingshan* 467036, *China*;
2. *Henan Province Key Laboratory of Water Pollution Control and Rehabilitation Technology*, *Henan University of Urban Construction*, *Pingdingshan* 467036, *China*）

Abstract: In this work we report the feasible modification of graphitic carbon nitride (g-C_3N_4) polymer through a post-functionalization progress. The resultant photocatalyst exhibits boron doping and mesoporous structure with a high surface area of 125 m^2/g, leading in an increased surface activity for photocatalytic water splitting reaction. X-ray diffraction, X-ray photoelectron spectroscopy, PL emission spectra and UV-Vis spectra were used to detect the properties of as-prepared samples. Based on X-ray photoelectron spectroscopy analysis, boron is proposed to dope in the g-C_3N_4 lattice. Optical studies indicated that boron doped g-C_3N_4 exhibits enhanced and extended light absorbance in the visible-light region and a much lower intensity of PL emission spectra compared to pure g-C_3N_4. As a result, boron doped g-C_3N_4 shows activity of 10.2 times higher than the pristine g-C_3N_4 for photocatalytic hydrogen evolution. This work may provide a way to design efficient and mesoporous photocatalysts through post modification.

Key words: boron-doping; mesoporous structure; post-functionalization; photocatalytic hydrogen evolution
CLC number: O644 **Document code:** A

The awareness of energy conservation and environmental protection has been roused due to the worldwide energy shortage and environmental issues, while numerous research focus on the exploration of renewable and clean energy[1]. Since the first discovery of photoelectrochemical (PEC) water splitting processing with titanium dioxide (TiO_2), semiconductor-based photocatalysis for solar hydrogen production has attracted global interests[2−4]. However, it is still challenging to achieve high solar-to-hydrogen (STH) conversion efficiency due to the restricted utilization of sunlight. To make good use of solar energy, the development of visible light responsive photocatalysts is highly desirable. In 2009, Wang et al.[5,6] developed graphitic carbon nitride (g-C_3N_4) for visible-light-driven photocatalytic water splitting, making it a hot research topic in the last decade.

Unlike TiO_2, g-C_3N_4 affords a narrow bandgap of ca. 2.7 eV with the conduction band (CB) position at ca. −1.1 eV and valance band (VB) position at ca. +1.6 eV vs. normal hydrogen electrode (NHE), respectively[5]. Furthermore, g-C_3N_4 photocatalyst possesses the advantages of stability, non-toxicity, abundant source, absorption in visible-light region and easy to control and modify. As a novel visible-light-driven photocatalyst, its remarkable property has been demonstrated in various photocatalytic applications such as H_2 and O_2 evolution[7−10], photodegradation of pollutants[11], CO_2 reduction[12], organic synthesis[13] and photoelectrocatalysis[14]. However, the three pivotal issues of light absorption efficiency, charge separation efficiency and surface reaction efficiency still limit the performance of g-C_3N_4-based photocatalysis. Therefore, it is highly desirable to modify g-C_3N_4 for efficient solar water splitting. Doping is considered as a very convenient and promising strategy to tune the band structure, enhance the lighting adsorption and improve the performance of photocatalyst[15]. Various doping strategies are employed to modify the g-C_3N_4 to improve the light harvesting, suppress the photogenerated charge recombination and enhance the photocatalytic activity. Combining g-C_3N_4 with strongly electronegative dopants such as fluorine to form an F-doped material not only raised the valence

Received: 2022-04-06; Revised: 2022-05-06

* Corresponding author. E-mail: ylyang@hncj.edu.com, 30010908@hncj.edu.cn.

The project was supported by Natural Science Youth Foundation of Henan Province (202300410032), Key Scientific Research Projects of Colleges and Universities of Henan Provincial Department of Education (21A150010), Foundation for University Key Teacher by the Henan University of Urban Construction (YCJQNGGJS202109).

本文的英文电子版由 Elsevier 出版社在 ScienceDirect 上出版 (http://www.sciencedirect.com/science/journal/18725813)

band, but also effected the thermodynamic driving force for H_2 reduction[16,17]. Fluorinated g-C_3N_4 solids was also reported with excellent visible-light photocatalytic activity[18]. Besides fluorine, I doping also lead positive effect like enlarged specific surface area, enhanced optical absorption, narrowed bandgap and accelerated charge carriers transfer rate as well as increased H_2 evolution rate[19]. Moreover, potassium-modified g-C_3N_4 (K-g-C_3N_4) nanosheets were synthesized[20]. Photocatalytic H_2 evolution experiments under visible light irradiation showed that K-g-C_3N_4 nanosheets have high photocatalytic activities (up to about thirteen times higher than that of pure g-C_3N_4) as well as good stability (no reduction in activity within 16 h). However, the doping methods have been reported mainly via calcination of precursors and doping source, which results in the bulk structure and heterogeneous distribution of doped ions and limited enhanced activity of photocatalysis. Therefore, it is of great importance to develop a feasible one-pot route for forming the porous structure and homogenizing the doping ions, which induces more reaction sites and optimizes the electronic structure. Furthermore, the selection of boron source may show significant effect on the doping sites and Lewis acidity on the surface of g-C_3N_4, which may also act as specific reaction sites for reactant molecules[21]. In particular, the textural, electronic, and structural properties of g-C_3N_4 can be modulated to boost the electron transfer and form a stable *p*-conjugation system. Thereby the doping and porous structure of g-C_3N_4 through a post-functionalization method may be feasible to achieve superior photocatalytic activity.

Herein, we report a facile strategy to synthesize porous B-doped g-C_3N_4 nanosheets by post-functionalization with PEI and Ph_4BNa. It is interesting to see that the resulted samples achieve boron doping and show porous structure simultaneously, while induce enhanced photocatalytic activity in photocatalytic hydrogen generation. As a result, an impressive H_2 production rate as high as 4280 μmol/(h·g) is achieved, which is 10.2 folds higher than that of pristine g-C_3N_4.

1 Experimental

1.1 Materials

Urea (CH_4N_2O), Tetraphenylboron sodium (Ph_4BNa, $(C_6H_5)_4BNa$), and triethanolamine ($C_6H_{15}NO_3$) were purchased from Sinopharm Chemical Reagent Beijing Co. Ltd. Polyethyleneimine ($(CH_2CH_2NH)_n$, M.W. 70000, 99%) were purchased from Alfa Aesar (China) Chemicals Co. Ltd. All chemicals were analytical grade and used as received without further purification.

1.2 Preparation of g-C_3N_4

The g-C_3N_4 powders were synthesized via the thermal polycondensation of urea according to the procedures described in literature[22]. In a typical synthesis, urea (10.0 g) sealed in a crucible was heated at a heating rate of 10 °C /min in a muffle furnace from room temperature (RT) to 550 °C and kept at this temperature for 4 h. The resulting yellow product was collected for further use.

1.3 Preparation of boron-doped g-C_3N_4

2 g g-C_3N_4 powders were immersed in 200 mL of DI water. Subsequent ultrasonication and vigorous stirring were applied to the prepared solutions for 0.5 and 12 h, respectively. After that, 0.2 g PEI was added to the above mixture. After continuously stirring for 1 h, suspension was separated through centrifugation at 10000 r/min, and the supernatants were poured out. The precursor solution of unmodified g-C_3N_4 was prepared by diluting the reserved solid into 200 mL of DI water. Then, 20 mg Ph_4BNa solution (1 mg/mL solution in DI water) was dropwise added to the above precursor solution of 20 mL while applying stirring for 1 h. The precursor precipitate was obtained by filtering and dried at 60 °C overnight for further synthesis. Boron-doped g-C_3N_4 was prepared by calcining the precursor precipitate, which was heated to 500 °C at a rate of 5 °C/min and maintained at 500 °C for 4 h in air. The B-doped g-C_3N_4 samples were denoted as BPCNX, in which X was the Ph_4BNa solution of 20, 50, 70, and 110 mg, respectively. For comparison purposes, another B-doped g-C_3N_4 (denoted as BCN) was also prepared by mixing the urea and Ph_4BNa directly without Ph_4BNa added according to the above procedures.

1.4 Characterization of B-doped g-C_3N_4

The samples were characterized using X-ray diffraction (Shimadzu XRD-7000 with Cu *K*α radiation, λ = 0.15418 nm), scanning electron microscopy (Hitachi S-8020U) and transmission electron microscopy (JEOL JEM-2010, operated at 200 kV). Nitrogen adsorption-desorption isotherms and pore-size distributions were measured on a Micromeritics ASAP 2020 at −196 °C. Specific surface areas and mean pore sizes were calculated according to the BET and Barrett-Joyner-Halenda (BJH) methods, respectively. A Shimadzu UV-

3100 PLUS spectrophotometer was used to measure the UV-visible (UV-Vis) absorption spectra of the samples. X-ray photoelectron spectroscopic (XPS) analysis was performed on a PHI Quantera SXM X-ray photoelectron spectrometer using the Al *K*α radiation. The photoluminescence (PL) spectra of g-C_3N_4 and B-doped g-C_3N_4 were recorded using the Edinburgh Instruments Xe900 equipped with a xenon (Xe) lamp with an excitation wavelength of 380 nm. The FT-IR spectrum was collected using a FT-IR-8400S spectrometer. Electrochemical and photoelectrochemical activities of samples were recorded on a CHI 660B electrochemical workstation in three-electrode quartz cells. A platinum electrode was used as the counter electrode, a saturated calomel electrode (SCE) was used as the reference electrodes, and g-C_3N_4 and B-doped g-C_3N_4 electrodes on FTO served as the working electrodes in 0.1 mol/L Na_2SO_4 aqueous solution. A 300 W Xe lamp (CHF-XW-300W) with a 420 nm cutoff filter was employed as the visible light source. The amperometric *i-t* curves of the samples were measured at 0 V with light on and light off. The electrochemical impedance spectra (EIS) were determined at 0 V. A sinusoidal ac signal of 5 mV was applied to the electrode in the frequency range of 1–100 kHz.

1.5 Photocatalytic experiments

Photocatalytic water splitting was carried out in a top-irradiation vessel connected to a LabSolar H_2 photocatalytic hydrogen evolution system (Perfectlight, Beijing) including a 300 W Xe lamp with a 420 nm cutoff filter. In a typical reaction, 50 mg of photocatalyst powder was dispersed in 100 mL aqueous solution containing 10% triethanolamine scavenger and 1% (respect to Pt, acting as co-catalysts) $H_2PtCl_6 \cdot 6H_2O$. The temperature of the reaction solution was carefully maintained at (5 ± 1) °C during the whole experiment. The reactor was then sealed and evacuated 40 min to remove air before irradiated. The amount of evolved H_2 was analyzed by gas chromatography (Agilent, 7890A GC system) equipped with a thermal conductive detector (TCD) and a 0.5 nm molecular sieve column, using high-purity nitrogen as the carrier gas.

2 Results and discussion

The crystal structure of g-C_3N_4 and B-doped g-C_3N_4 photocatalysts were examined by XRD, as illustrated in Figure 1(a). The diffractogram of the samples featured two distinct (100) and (002) reflections at 2θ = 13.08º and 27.58º, corresponding to an in-plane structural packing motif and the long-range interplanar stacking of the conjugated aromatic system, respectively[23]. The XRD patterns of BPCN samples were similar to that of pristine g-C_3N_4, however, as for the doped samples, the intensity of the (002) crystal plane reduced substantially with the increase of boron amount, and the (002) diffraction of BPCN-110 (the heaviest doped g-C_3N_4) was significantly weakened, which can be attributed to the presence of excessive B atoms doping in the graphitic structure. This can be an evidence for the successful doping in g-C_3N_4. The morphology of the as-prepared g-C_3N_4 samples was examined by field-emission SEM (FE-SEM). The SEM image of BPCN-70 in Figure 1(b) showed a clearly wrinkle 2D structure. As shown in inset of Figure 1(b), the nanosheet was composed of uniform distributed C, N, B and O elements, indicating that B elements were homogeneously doped in g-C_3N_4. The nanostructures of g-C_3N_4 and BPCN-70 were characterized by transmission electron microscopy (TEM). BPCN-70 showed thin nanosheet structure with mesoporous structure (Figure 1(c)), indicating that the post-functionalization process developed in this work can achieve the delamination and formation of mesopore. This thin nanosheet and uniform mesoporous structure was highly desirable for photocatalytic reaction because the thin layer reduced the distance of charge transfer and pore structure can provide the photocatalytic activity sites. To further confirm the mesopore structure of B-doped g-C_3N_4, textural properties of g-C_3N_4 and BPCN-70 were investigated by the nitrogen adsorption-desorption measurement. The obtained absorption isotherms and Barrett-Joyner-Halenda (BJH) pore-size distributions were shown in Figure 1(d). The adsorption-desorption isotherm of these two samples have been classified as type IV with a H3 hysteresis loop, which was characteristic of mesoporous materials with slit-shaped pores[24]. The surface area (S_{BET}) and pore volume of BPCN-70 was calculated as to be 125 m^2/g and 0.35 cm^3/g, whereas that of g-C_3N_4 was 101 m^2/g and 0.49 cm^3/g. It was reasonable to state that the increased BET surface area was mainly derived from post-functional treatment, which would provide more active sites for photocatalytic hydrogen evolution. The pore-size distribution curves calculated using the BJH model clearly showed that g-C_3N_4 material had two pore-size families located at 3.9 and 30−50 nm, while the

primary pore size of BPCN-70 was centered at 13 nm (inset of Figure 1(d)), which agreed well with that estimated from TEM images. This pore structure was attributed to the formation of uniform mesoporous structure. These results indicated that the post-functionalization of g-C_3N_4 yielded a large surface area and mesoporosity. B-doped g-C_3N_4 prepared by other doping amount presented regular S_{BET} values, which were 116, 110, 99 m^2/g for the BPCN-20, BPCN-50 and BPCN-110 samples, respectively.

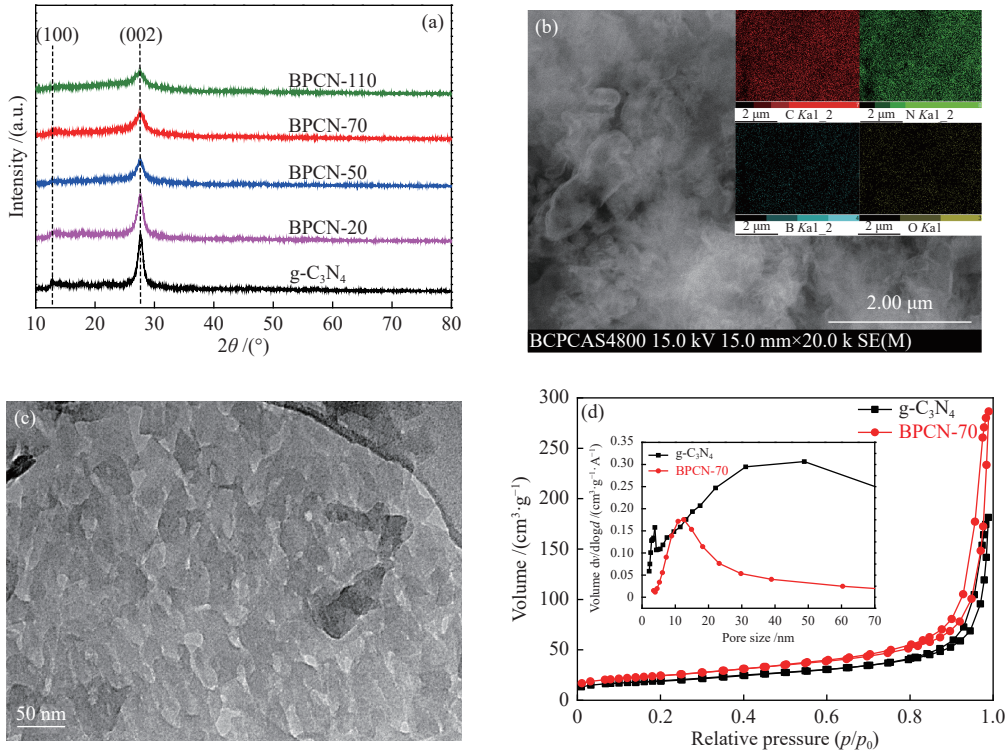

Figure 1 (a) XRD patterns of g-C_3N_4 and BPCN samples; (b) SEM and (c) TEM image of BPCN-70 nanosheet, inset in (b): the element mapping of C, N, B and O for BPCN-70, respectively; (d) Nitrogen adsorption-desorption isotherms, inset: pore size distributions of g-C_3N_4 and BPCN-70

Figure 2(a) depicted the absorbance spectra of g-C_3N_4 and B-doped g-C_3N_4, which all featured a notable absorption extending from UV part to the visible light region. In comparison with that of g-C_3N_4, there was a little red shift of the absorption in BCN and BPCN samples, which may due to the existence of Boron species. The band gaps of g-C_3N_4, BCN-70 and BPCN-70 materials were 2.92, 2.87 and 2.72 eV. BPCN-70 exhibited typical VB characteristics of g-C_3N_4, with the VBM energy at about 1.51 eV versus RHE[25]. Since the band gap of BPCN-70 was 2.72 eV from the optical measurement, the CBM can be estimated at about −1.21 eV. As a result, the material gap can be narrowed and the ability of BPCN-70 to harvest visible light can be improved with this post-functional modification. The improved photoabsorption property demonstrated that more electrons generated and participated in the photocatalytic reaction, which can result in enhanced photocatalytic activity.

The chemical structure of g-C_3N_4 nanosheets was confirmed by the FT-IR spectra shown in Figure 2(b). The broad peaks between 3500 and 3000 cm^{-1} originating from the N−H stretches can be clearly observed, suggesting the partial hydrogenation of some nitrogen atoms in the nanosheets. Characteristic bands of aromatic CN heterocycles are at 1200 to 1600 cm^{-1} and 802 cm^{-1} is characteristic of s-triazine derivatives[24,26]. Specifically, the vibrations of the B-related group (N-B-N) were observed at 1370 cm^{-1} in the doped CN matrix, despite overlapped of the band with that of the C−N vibrations[27]. Clearly, the FT-IR spectrum of B doped g-C_3N_4 nanosheets was similar to that of original g-C_3N_4, indicating that the B doped g-C_3N_4 nanosheets keep the same chemical structure as their parent g-C_3N_4. Furthermore, the thermogravimetric analysis (TGA-DSC) has been performed to analyze the stability of BPCN-70, as shown in Figure 2(c). The first stage with 8.75% mass loss corresponds to the release of water molecules adsorbed and oxygen-containing groups[28]. When the

temperature was higher than 500 °C, the structure of BPCN-70 began to break up and BPCN-70 sample can be completely decomposed into small molecules such as C_2N_2 and NH_3[29]. In addition, the temperature for the maximum endothermic peak of BPCN-70 was at 684 °C, resulting in a strong thermal stability.

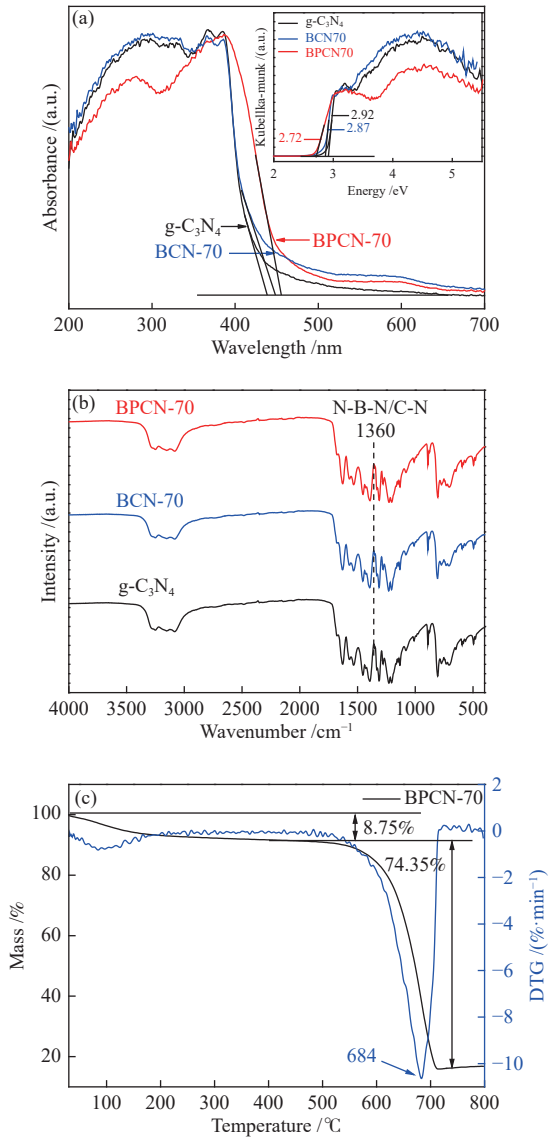

Figure 2　(a) UV-Visible diffuse reflectance spectra of g-C_3N_4, BCN-70 and BPCN-70 samples; inset: transformed Kubelka-Munk function versus the energy spectra of g-C_3N_4, BCN-70 and BPCN-70 samples; (b) FT-IR spectra of g-C_3N_4, BCN-70 and BPCN-70 samples; (c) TG spectra of BPCN-70

To further determine the incorporation of B atoms and their oxidation state in the CN framework, The XPS analysis was performed and the results are shown in Figure 3. The XPS survey spectrum in Figure 3(a) showed that the sample contains only C, N and O species without other impurities, while peak of B cannot be noted in the survey spectrum due to the lower intensity compared to that of N specie. A clear B 1*s* XPS peak with a binding energy (E_B) of 191.88 eV was observed for the BPCN-70 sample (Figure 3 (b)), corresponding to N-B-N coordination in the unit of heptazine[30]. This indicated that some of the B atoms were introduced into the carbon sites of CN matrix. The C 1*s* spectrum (Figure 3(c)) of the BPCN-70 sample displayed two peaks at E_B = 285.48 and 288.88 eV, which was attributed to contaminated carbon and surface carbon, and the C-(N)3 groups of g-C_3N_4, respectively[31]. Figure 3(d) showed the N 1*s* XPS spectrum of the BPCN-70. This spectrum has been fitted to four peaks, which are attributed to the sp^2-hybridized nitrogen (C−N=C) species at E_B = 399.08 eV, the N-(C)3 species at E_B = 400.08 eV, the quaternary N bonded to three C atoms in the aromatic cycles at E_B = 401.02 eV and charging effects at E_B = 404.58 eV[32]. According to the XPS and FT-IR analyses, it was concluded that the boron element was indeed doped in g-C_3N_4 nanosheets.

The photocatalytic H_2 production activity of B doped g-C_3N_4 was evaluated and compared with g-C_3N_4. As shown from H_2 production rates over B doped g-C_3N_4 samples with different B contents (Figure 4(a)), the photocatalytic H_2 production rate increased dramatically with B doping. It reached maximum 4280 μmol /(h·g) over BPCN-70 that showed 10.2-fold improvement in comparison with pure g-C_3N_4 (420 μmol/(h·g)). The H_2-evolution rate achieved in this work was one of the best for boron doped g-C_3N_4 (Table 1). Moreover, the long-term ability of BPCN-70 was further evaluated (Figure 4(b)). The recycle kinetics curves demonstrated a slight deactivation with time in the first five runs. When an appropriate amount of triethanolamine (TEOA) was added to the reaction solution, BPCN-70 can maintain sustainably stable photocatalytic H_2 production rate over 5 cycles accumulated 20 h, which indicate that it has the good durability and reusability. The photocatalytic performance of g-C_3N_4, BPCN-70 and BCN-70 with no cocatalyst was shown in Figure 5(c). g-C_3N_4 presented a H_2-generation rate of 70 μmol/(h·g), which is much lower than that with Pt. Similarity, with no Pt as cocatalyst, the BPCN-70 sample still presented the fastest H_2-production rate of 610 μmol/(h·g), which approaches 8.7 times that of pure g-C_3N_4. Additionally, this value is also higher than that of the BCN-70 (220 μmol/(h·g)).

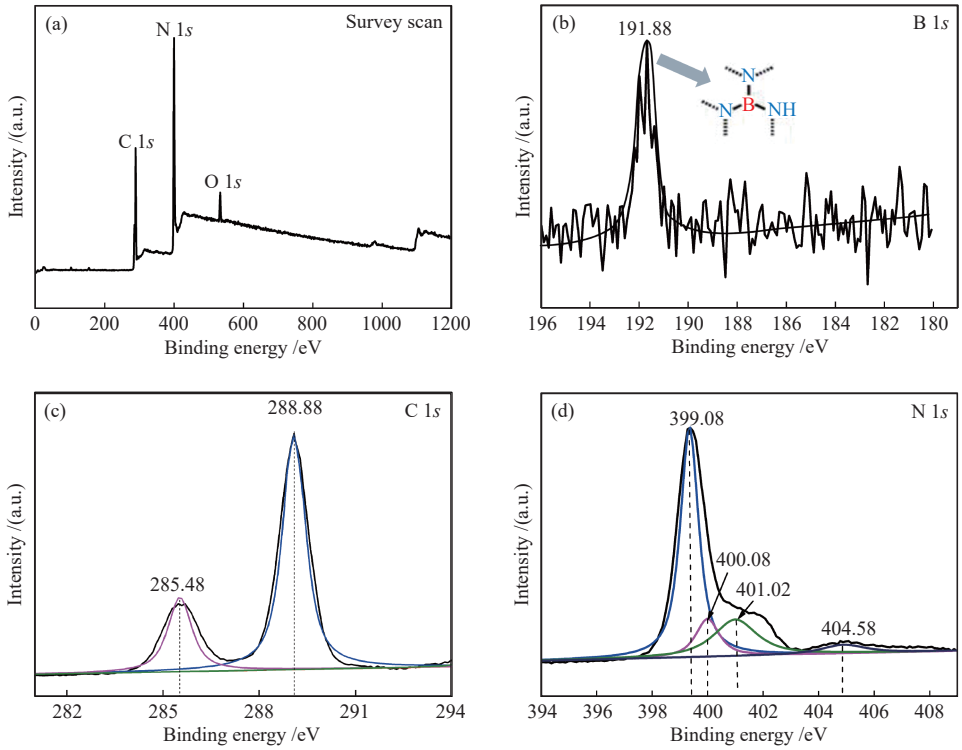

Figure 3 ((a), (b), (c) and (d)) XPS spectra of survey, B 1*s*, C 1*s* and N 1*s*, respectively, for BPCN-70 sample

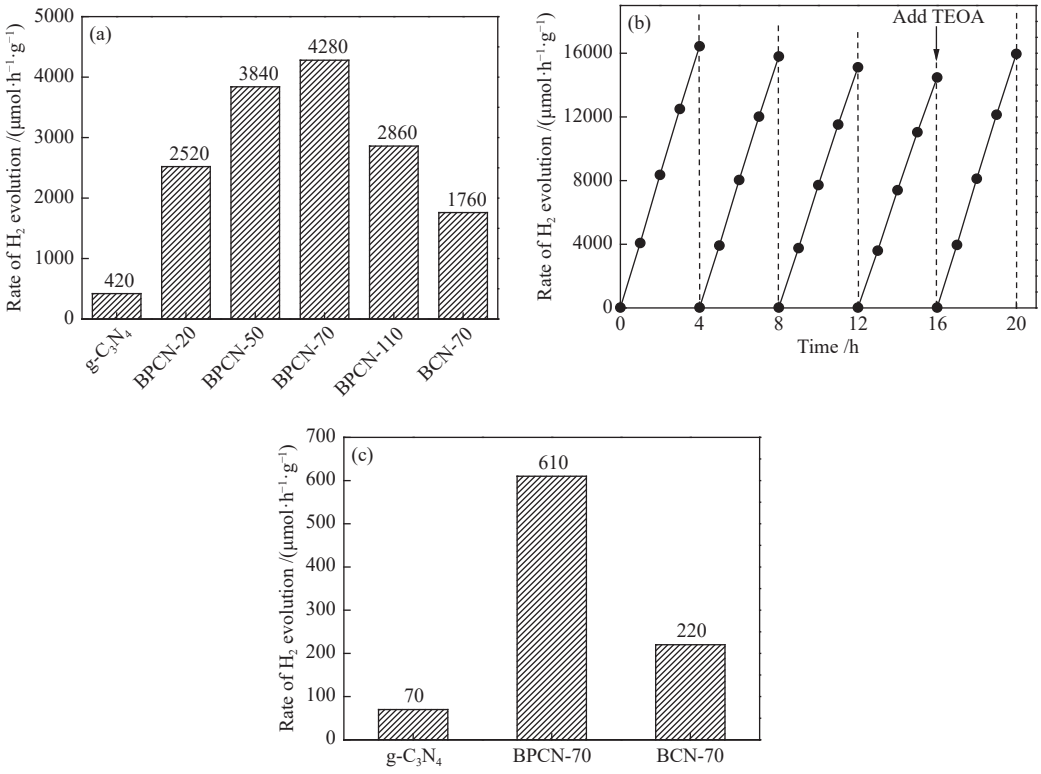

Figure 4 (a) Photocatalytic H_2-generation activity over the typical samples with 1% Pt as cocatalyst; (b) cyclic running kinetics curves of H_2 production over BPCN-70; (c) photocatalytic H_2-generation activity over the typical samples with no cocatalyst

Table 1　Summary of recent result in boron doped g-C_3N_4 for solar water splitting

Sample	H_2-evolution rate/(μmol·h^{-1}·g^{-1})	Condition	Ref.
1	1880	1% Pt, 300 W Xe lamp with a 400 nm cutoff filter	[33]
2	3880	1% Pt, A Xe lamp (350 nm < λ < 780 nm)	[34]
3	1439	1% Pt, 300 W Xe lamp	[35]
4	704.5	3% Pt, 300 W Xe lamp with 420 nm cutoff filter	[36]
5	278	3% Pt, 300 W Xe lamp with 420 nm cutoff filter	[27]
6	4280	1% Pt, 300 W Xe lamp with 420 nm cutoff filter	this work

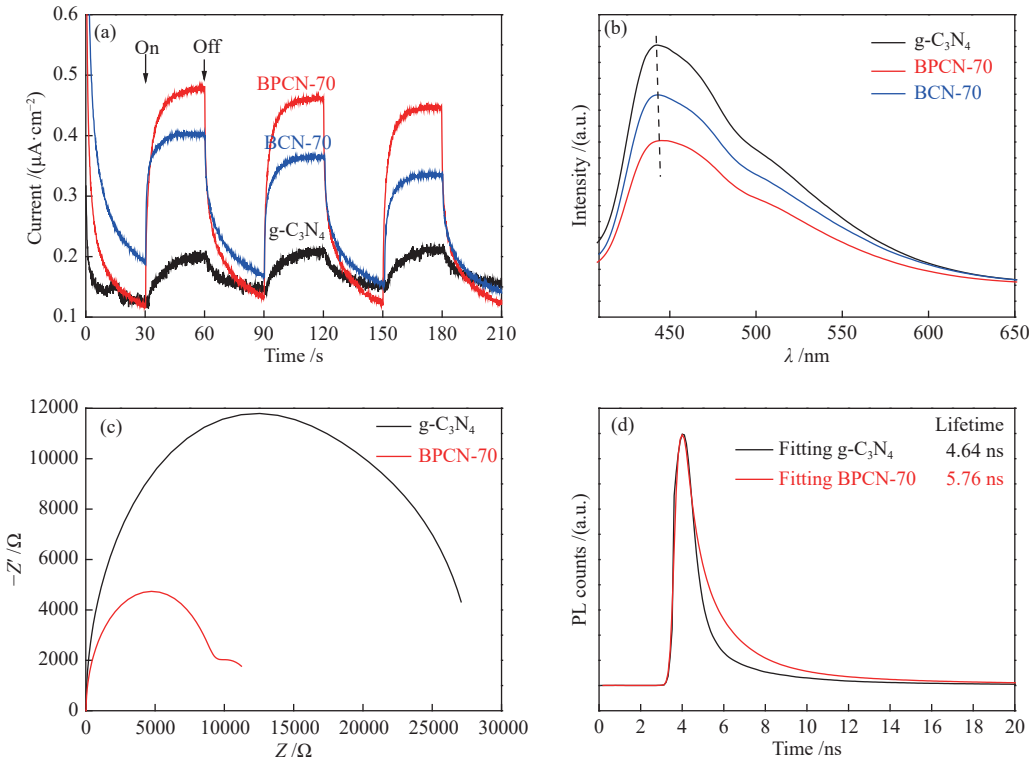

Figure 5　(a) transient photocurrent density versus time; (b) photoluminescence spectra; (c) EIS Nyquist plots; (d) time-resolved transient PL spectra of typical samples

To further investigate the underlying mechanism for improved photocatalytic activity, the effect of doping species on the charge carrier migration and separation behaviors were investigated by transient photocurrent responses, EIS and PL spectra. Seen from Figure 5(a), BPCN-70 produced the continually stable transient photocurrent response during the three on/off intermittent irradiation cycles over 210 s under the visible light. It can be seen that the photocurrent of BPCN-1 sample was about 2.4 and 1.2 times higher than that of g-C_3N_4 and BCN-70, respectively, suggesting that B doping species by post-modification can efficiently promote the carrier separation and the enhanced photocatalytic activity can be ascribed to the significantly improved photogenerated charge separation efficiency. PL spectra of B doped g-C_3N_4 and g-C_3N_4 samples were recorded at an excitation wavelength of 380 nm to determine the transfer and separation efficiency of photogenerated electron–hole pairs[37]. As shown in Figure 5(b), the main emission band was centered at about 460 nm for pure g-C_3N_4, which was due to the recombination process of self-trapped excitation[38]. The emission peak positions of BCN-70 and BPCN-70 samples were similar to those of g-C_3N_4. However, the emission intensity of BPCN-70 composite sample was lower than that of pristine g-C_3N_4 and BCN-70. This result clearly indicates that the recombination of photogenerated charge carriers was inhibited and B-doping into the g-C_3N_4 lattice contributed to the separation of photoinduced charge carriers, which was in agreement with the photocatalytic H_2 evolution results. Moreover, the EIS

spectra in Figure 5(c) presented that the lesser arc radius of Nyquist plot was produced on BPCN-70 electrode compared with g-C_3N_4, proving that the charge carrier recombination was suppressed and interfacial charge transfer ability was promoted effectively, leading to a higher photocatalytic hydrogen production performance. The time-resolved transient PL spectra in Figure 5(d) were further carried out to investigate charge separation behaviors. The fitted fluorescence lifetime increased from 4.64 ns of g-C_3N_4 to 5.76 ns of BPCN-70, which further verified that the doped B significantly prolonged the PL lifetime and hindered the annihilation of charge carriers. Thus, more electrons can participate in the photocatalytic H_2-evoultion reaction, which may enhance the performance of BPCN.

Based on the above results, the post-functionalization process can achieve B-doping into the structure and induce formation of mesoporous structures. The synergistic effect of element doping and mesostructured controlling promotes charge carrier separation and transfer, leading to an enhanced photocatalytic activity.

To gain insight into the stability of BPCN-70, XRD and FT-IR are carried out on BPCN-70 after cycle runs. It can be noted that no obvious change in material structures was observed through XRD and FT-IR examinations (Figure 6(a) and 6(b)) for the sample before and after reaction. This indicates that the decrease in the activity after the first run is mainly due to the decreased concentration of triethanolamine. Based on the above discussion, it is reasonable to conclude that the structure of g-C_3N_4 with post-functional modification is quite stable.

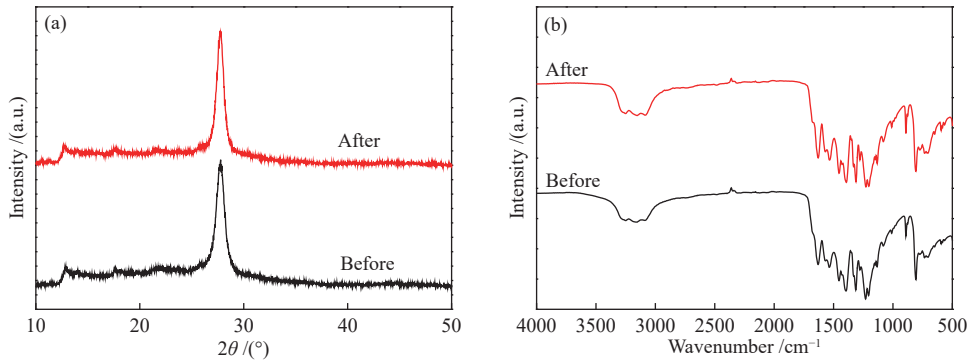

Figure 6 (a) XRD patterns of BPCN-70; (b) FT-IR spectra of BPCN-70 before and after hydrogen evolution reaction

3 Conclusions

In summary, a feasible post-functionalization method has been applied to modify g-C_3N_4 to achieve B doping and mesoporous structure, which exhibited enhanced photocatalytic hydrogen production performance. The superior photocatalytic activity and stability were ascribed to the greatly improved charge migration and separation ability. The optimized BPCN-70 exited optimal H_2 production rate of 4280 μmol/(h·g) that was 10.2-fold improved in comparison with pristine g-C_3N_4 (420.0 μmol/(h·g)). Meanwhile, the cycle running experiments indicated that BPCN-70 had good stability and reusability. The findings demonstrate a useful strategy to achieve element doping and structure controlling simultaneously for enhanced photocatalytic performance.

References

[1] GIELEN D, BOSHELL F, SAYGIN D. Climate and energy challenges for materials science[J]. Nat Mater, 2016, **15**: 117−120.

[2] FUJISHIMA A, HONDA K. Electrochemical photolysis of water at a semiconductor electrode[J]. Nature, 1972, **238**: 37−38.

[3] CHEN F, MA T, ZHANG T, ZHANG Y, HUANG H. Atomic-level charge separation strategies in semiconductor-based photocatalysts[J]. Adv Mater, 2021, **23**(10): 2005256.

[4] YANG Y, WANG S, LI Y, WANG J, WANG L. Strategies for efficient solar water splitting using carbon nitride[J]. Chem Asian J, 2017, **12**: 1421−1434.

[5] WANG X, MAEDA K, THOMAS A, TAKANABE K, XIN G, CARLSSON J M, DOMEN K, ANTONIETTI M. A metal-free polymeric photocatalyst for hydrogen production from water under visible light[J]. Nat Mater, 2009, **8**: 76−80.

[6] XING Y, WANG X, HAO S, ZHANG X, WANG X, MA W, ZHAO G, XU X. Recent advances in the improvement of g-C_3N_4 based photocatalytic materials[J]. Chin Chem Lett, 2021, **32**(1): 13−20.

[7] HAN C, SU P, TAN B, MA X, LV H, HUANG C, WANG P, TONG Z, LI G, HUANG Y, LIU Z. Defective ultra-thin two-dimensional g-C_3N_4 photocatalyst for enhanced photocatalytic H_2 evolution activity[J]. J Colloid Interfaces Sci, 2021, **581**: 159−166.

[8] LI J, LIU X, CHE H, LIU C, LI C. Facile construction of O-doped crystalline/non-crystalline g-C_3N_4 embedded nano-homojunction for efficiently photocatalytic H_2 evolution[J]. Carbon, 2021, **172:** 602−612.
[9] ZHU B, CHENG B, FAN J, HO W, YU J. g-C_3N_4-based 2D/2D composite heterojunction photocatalyst[J]. Small, 2021, **2:** 2100086.
[10] YU X, NG S-F, PUTRI L K, TAN L-L, MOHAMED A R, ONG W-J. Point-defect engineering: Leveraging imperfections in graphitic carbon nitride (g-C_3N_4) photocatalysts toward artificial photosynthesis[J]. Small, 2021, **17:** 2006851.
[11] ZHANG H, FENG L, LI C, WANG L. Preparation of graphitic carbon nitride with nitrogen-defects and its photocatalytic performance in the degradation of organic pollutants under visible light[J]. J Fuel Chem Technol, 2018, **46**(7): 871−878.
[12] YUAN J, YI X, TANG Y, LIU C, LUO S. Efficient photocatalytic hydrogen evolution and CO_2 reduction: enhanced light absorption, charge separation, and hydrophilicity by tailoring terminal and linker units in g-C_3N_4[J]. ACS Appl Mater Interfaces, 2020, **12:** 17,19607−19615.
[13] CAMUSSI I, MANNUCCI B, SPELTINI A, PROFUMO A, MILANESE C, MALAVASI L, QUADRELLI P. g-C_3N_4-singlet oxygen made easy for organic synthesis: scope and limitations[J]. ACS Sustainable Chem Eng, 2019, **7:** 9,8176−8182.
[14] TRUONG H B, BAE S, CHO J, HUR J. Advances in application of g-C_3N_4-based materials for treatment of polluted water and wastewater via activation of oxidants and photoelectrocatalysis: A comprehensive review[J]. Chemosphere, 2022, **286:** 131737.
[15] PATNAIK S, SAHOO D P, PARIDA K. Recent advances in anion doped g-C_3N_4 photocatalysts: A review[J]. Carbon, 2021, **172:** 682−711.
[16] WANG H, ZHANG X, XIE J, ZHANG J, MA P, PAN B, XIE Y. Structural distortion in graphitic-C_3N_4 realizing an efficient photoreactivity[J]. Nanoscale, 2015, **7:** 5152−5156.
[17] SHEVLIN S A, GUO Z X. Anionic dopants for improved optical absorption and enhanced photocatalytic hydrogen production in graphitic carbon nitride[J]. Chem Mater, 2016, **28:** 7250−7256.
[18] YE H, WANG Z, YU F, ZHANG S, KONG K, GONG X, HUA J, TIAN H. Fluorinated conjugated poly(benzotriazole)/g-C_3N_4 heterojunctions for significantly enhancing photocatalytic H_2 evolution[J]. Appl Catal B: Environ, 2020, **267:** 118577.
[19] IQBAL W, YANG B, ZHAO X, RAUF M, MOHAMED I M A, ZHANG J, MAO Y. Facile one-pot synthesis of mesoporous g-C_3N_4 nanosheets with simultaneous iodine doping and N-vacancies for efficient visible-light-driven H_2 evolution performance[J]. Catal Sci Technol, 2020, **10:** 549−559.
[20] WANG Y, ZHAO S, ZHANG Y, FANG J, ZHOU Y, YUAN S, ZHANG C, CHEN W. One-pot synthesis of K-doped g-C_3N_4 nanosheets with enhanced photocatalytic hydrogen production under visible-light irradiation[J]. Appl Surf Sci, 2018, **440:** 258−265.
[21] SHI Y K, HU X J, CHEN L, LU Y, ZHU B L, ZHANG S M, HUANG W P. Boron modified TiO_2 nanotubes supported Rh-nanoparticle catalysts for highly efficient hydroformylation of styrene[J]. New J Chem, 2017, **41:** 6120−6126.
[22] CHEN F, WU C, ZHENG G, QU L, HAN Q. Few-layer carbon nitride photocatalysts for solar fuels and chemicals: Current status and prospects[J]. Chin J Catal, 2022, **43:** 1216−1229.
[23] ZHANG J, ZHANG G, CHEN X, LIN S, MÇHLMANN L, DOŁEGA G, LIPNER G, ANTONIETTI M, BLECHERT S, WANG X. Co-monomer control of carbon nitride semiconductors to optimize hydrogen evolution with visible light[J]. Angew Chem Int Ed, 2012, **51:** 3183−3187.
[24] SING K S W, EVERETT D H, HAUL R A W, MOSCOU L, PIEROTTI R A, ROUQUEROL J, SIEMIENIEWSKA T. Reporting physisorption data for gas/solid systems with special reference to the determination of surface area and porosity[J]. Pure Appl Chem, 1985, **57:** 603−619.
[25] YU H, SHI R, ZHAO Y, BIAN T, ZHAO Y, ZHOU C, WATERHOUSE G I N, WU L Z, TUNG C-H, ZHANG T. Alkali-assisted synthesis of nitrogen deficient graphitic carbon nitride with tunable band structures for efficient visible-light-driven hydrogen evolution[J]. Adv Mater, 2017, **29:** 1605148.
[26] WANG Y, WANG X, ANTONIETTI M. Polymeric graphitic carbon nitride as a heterogeneous organocatalyst: from photochemistry to multipurpose catalysis to sustainable chemistry[J]. Angew Chem Int Ed, 2012, **51:** 68−69.
[27] LIN Z, WANG X. Nanostructure engineering and doping of conjugated carbon nitride semiconductors for hydrogen photosynthesis[J]. Angew Chem Int Ed, 2013, **52:** 1735−1738.
[28] WU X, CHEN F, WANG X, YU H. In situ one-step hydrothermal synthesis of oxygen-containing groups-modified g-C_3N_4 for the improved photocatalytic H_2-evolution performance[J]. Appl Surf Sci, 2018, **427:** 645−653.
[29] LAU V W-H, MESCH M B, DUPPEL V, BLUM V, SENKER J, LOTSCH B V. Low-molecular-weight carbon nitrides for solar hydrogen evolution[J]. J Am Chem Soc, 2015, **137:** 1064−1072.
[30] WANG Y, LI H R, YAO J, WANG X C, Antonietti M. Synthesis of boron doped polymeric carbon nitride solids and their use as metal-free catalysts for aliphatic C–H bond oxidation[J]. Chem Sci, 2011, **2:** 446−450.
[31] MIRAND C, MANSILLA H, Y´ANEZ J, OBREGON S, COLONA G. Improved photocatalytic activity of g-C_3N_4/TiO_2 composites prepared by a simple impregnation method[J]. J Photochem Photobiol A, 2013, **253:** 16−21.
[32] CHAI B, PENG T, MAO J, LI K, ZAN L. Graphitic carbon nitride (gC_3N_4)-Pt-TiO_2 nanocomposite as an efficient photocatalyst for hydrogen production under visible light irradiation[J]. Phys Chem Chem Phys, 2012, **14:** 16745−16752.
[33] THAWEESAK S, WANG S, LYU M, XIAO M, PEERAKIATKHAJOHN P, WANG L. Boron-doped graphitic carbon nitride nanosheets for enhanced visible light photocatalytic water splitting[J]. Dalton Trans, 2017, **46:** 10714−10720.
[34] WANG X, LIU B, XIAO X, WANG S, HUANG W. Boron dopant simultaneously achieving nanostructure control and electronic structure tuning of graphitic carbon nitride with enhanced photocatalytic activity[J]. J Mater Chem C, 2021, **9:** 14876−14884.
[35] CHEN P, XING P, CHEN Z, LIN H, HE Y. Rapid and energy-efficient preparation of boron doped g-C_3N_4 with excellent performance in photocatalytic H_2-evolution[J]. Inter J Hydrogen Energy, 2018, **43:** 19984−19989.
[36] LUO Y, WANG J, YU S, CAO Y, MA K, PU Y, ZOU W, TANG C. Nonmetal element doped g-C_3N_4 with enhanced H_2 evolution under visible light irradiation[J]. J Mater Res, 2018, **33:** 1268−1278.

[37] MARTHA S, NASHIM A, PARIDA K M. Facile synthesis of highly active g-C_3N_4 for efficient hydrogen production under visible light[J]. J Mater Chem A, 2013, **1**: 7816−7824.

[38] ONG W J, TAN L L, CHAI S P, YONG S T, MOHAMED A R. Surface charge modification via protonation of graphitic carbon nitride (g-C_3N_4) for electrostatic self-assembly construction of 2D/2D reduced graphene oxide (rGO)/g-C_3N_4 nanostructures toward enhanced photocatalytic reduction of carbon dioxide to methane[J]. Nano Energy, 2015, **13**: 757−770.

基于后功能化工艺修饰类石墨相氮化碳及其光催化产氢性能研究

杨亦龙[1,*]，李山鹰[1]，毛艳丽[2]，党丽赟[1]，焦卓凡[1]，徐开东[1,*]

（1. 河南城建学院 材料与化工学院, 河南 平顶山 467036;

2. 河南城建学院 河南省水体污染防治与修复重点实验室, 河南 平顶山 467036）

摘　要: 本研究设计了一种后功能化工艺方法修饰类石墨相氮化炭材料。通过此工艺成功得到了硼掺杂的介孔氮化炭材料, 该材料比表面积高达 125 m^2/g, 这为提升光催化分解水性能奠定了基础。利用 X 射线衍射、X 射线光电子能谱, 荧光光谱和紫外-可见光谱对材料进行了全面的表征。基于 X 射线光电子能谱分析, 发现通过后功能化处理硼原子成功掺杂进入氮化炭的晶格中; 通过吸收光谱分析得知, 硼掺杂的介孔氮化炭材料增强了在可见光区的光吸收; 通过荧光光谱分析得知, 相比原始氮化炭材料, 硼掺杂后的介孔氮化炭材料有着更低的荧光强度, 意味着光生电子和空穴的分离得到了提升。对材料进行光催化分解水测试, 后功能化处理得到的硼掺杂介孔氮化炭材料的产氢速率是原始氮化炭材料的 10.2 倍。此结论对后续利用后功能化工艺修饰材料提升材料性能具有一定的借鉴意义。

关键词: 硼掺杂; 介孔结构; 后功能化; 光催化产氢

中图分类号: O644　　**文献标识码:** A